AIAA No. 98-0490
An Experimental And Computational Investigation of Spanwise-Step-Ice Shapes on Airfoil Aerodynamics

S. Lee, T. Dunn, H.M. Gurbacki, M.B. Bragg and E. Loth
University of Illinois at Urbana-Champaign
Urbana, IL

36th Aerospace Sciences Meeting & Exhibit
January 12–15, 1998 / Reno, NV

AN EXPERIMENTAL AND COMPUTATIONAL INVESTIGATION OF SPANWISE-STEP-ICE SHAPES ON AIRFOIL AERODYNAMICS

Sam Lee*, Tim Dunn*, Holly Gurbacki*, Mike Bragg** and Eric Loth***
University of Illinois at Urbana-Champaign, Urbana, IL 61801

ABSTRACT

The objective of this research was to study the effects of spanwise-step-ice accretions (resulting from large droplet icing conditions) on subsonic aircraft aerodynamics. The airfoil investigated was a modified NACA 23012 with a simple flap. An experimental and computational program was conducted using simulated ice accretions to determine the sensitivity of ice shape size and location on airfoil performance and control as a function of angle of attack and flap deflection. Focus is paid on the critical conditions where the aerodynamic performance, and the hinge moment in particular, changes rapidly and non-linearly. The experimental program included wake surveys, surface pressure taps, and force-balance measurements to obtain lift, drag, pitching moment, and hinge-moment coefficients for a large variety of geometry and flow conditions. The accompanying computational investigation was performed with a high-resolution full Navier-Stokes solution using a solution-adaptive unstructured grid for both non-iced and iced configurations. Results are presented for experiments and predictions of sectional aerodynamic characteristics where the quarter-round ice shape heights of 0.0083 and 0.0139 chords resulted in a dramatic decrease in maximum lift coefficients as well as significant reductions in hinge moments for positive angles of attack.

INTRODUCTION

The crash of an ATR-72 commuter aircraft near Roselawn, Indiana on October 31, 1994, has led to much reevaluation of our current understanding of aircraft icing. The accident is thought to have occurred due to the presence of freezing drizzle which consisted of droplet sizes much larger than those in the FAR Part 25, Appendix C icing envelopes. Dow provided an excellent overview of the accident and its causes in his 1995 article.[1]

Ice accretions due to large-droplet icing can occur on the upper surface behind the active portion of the de-icing system boot and can lead to a spanwise-step type of ice accretion protuberance.[2] This can lead to changes in the lateral control, and the associated hinge moments, of the aircraft by altering the flow over the ailerons. It is this degradation in aileron control that is thought to have led to the Roselawn accident. Although the accident is thought to have occurred due to the presence of supercooled large droplets (SLD) and subsequent loss of aileron control, the problem is more general. This type of ice accretion can also occur in supercooled droplet clouds of Appendix C size droplets when the air temperature is near freezing. In this case, the accretion occurs behind the boot due to surface water runback, and not due to impingement in this region. Also, spanwise-step-ice accretion is not limited to the wing and aileron, but could also occur on the horizontal and vertical tail and affect other control surfaces including the elevator and rudder, respectively.

The influence of ice accretion behind de-icing boots on aircraft performance has long been recognized. Wind tunnel measurements by Johnson[3] in 1940 showed a 36% reduction in maximum roll control power due to ice accretion with full aileron deflection. However, the study did not focus on hinge moments or control forces, and no analysis of the cause of this effect, or documentation of the simulated ice shape or icing conditions were presented. As a response to a Viking aircraft incident, in 1947 Morris[4] reported wind tunnel results of the effect of simulated ice shapes on the leading edge of the aircraft horizontal tail. The objective was to propose a fix for the elevator control. One of the simulated ice shapes resembles an SLD accretion, and was intended to represent ice formed downstream of a de-icing system. Hinge moment results are summarized and design guidelines are presented. In 1948 Thoren[5] documented a 2-hour test flight in freezing rain with a Lockheed P2V aircraft. During this encounter, runback and freezing were observed behind the boots. A considerable increase in section drag and a reduction in lift were noted, but no serious degradation in lateral control was experienced. Thus by 1950 it seems clear that there existed a basic understanding that ice accretion aft of the boots could affect aircraft control.

Research at the University of Wyoming has considered the aerodynamic effects of various types of ice accretion. During flight tests of the King Air aircraft, Cooper et al.[6] experienced two icing encounters with droplet sizes of 30 μm to 300 μm. Aircraft performance

* Graduate Research Assistant, Department of Aeronautical and Astronautical Engineering, Student Member AIAA
** Professor, Department of Aeronautical and Astronautical Engineering, Associate Fellow of AIAA
*** Associate Professor, Department of Aeronautical and Astronautical Engineering, Senior Member of AIAA

losses for these cases were "anomalously large although the liquid water content (LWC) and median volume diameter (MVD) did not indicate that these cases should have been potentially hazardous." Recently Ashenden and Marwitz[7] analyzed several Wyoming King Air flights in icing to determine the effect of various icing encounters on aircraft performance. They report that freezing drizzle exposure resulted in the maximum rate of performance degradation of all icing cases studied. Ashenden, Lindberg and Marwitz[8] found a similar result in 2-D wind tunnel tests. They conducted low Reynolds number wind tunnel tests on an airfoil with simulated freezing drizzle and freezing rain ice accretions. The ice shapes were predicted using the LEWICE computer code. The results showed more severe aerodynamic penalties due to the freezing drizzle case when operation of the deicing boot was simulated. However, aircraft control problems due to freezing drizzle were not addressed in detail in this work.

Initial insight into the effect of SLD ice accretion on aircraft control can be found in the excellent report on horizontal tail stall by Trunov and Ingelman-Sundberg.[9] The combination of increased downwash due to main wing flap deflection and decreased maximum lift and stall angle due to ice on the horizontal tail can lead to horizontal tail stall. They reported hinge-moment data on airfoils and tail sections with simulated ice accretions and argued that the change in airfoil pressure distribution over the elevator due to the ice-induced separation led to altered hinge moments and pilot control forces. This study thoroughly addressed the cause of the horizontal tail stall problem on aircraft longitudinal control and explained the cause of many such aircraft accidents. Trunov and Ingelman-Sundberg do not, however, address in detail the aerodynamics of this phenomena or consider the large spanwise-step type of ice typically found aft of ice protection in SLD conditions.

In 1996 Bragg[10,11] reviewed the aerodynamic effects of large-droplet ice accretion on aircraft aerodynamics and lateral control based in part on horizontal tail stall data.[9, 12] The spanwise-step-ice accretion, thought to be typical of SLD ice, was shown to not only degrade lift and drag, but to also adversely affect the aileron hinge moment. This hinge moment effect was traced to the change in the airfoil pressure distribution caused by the separation induced by the ice accretion. However, the authors are unaware of detailed aerodynamic data for spanwise-step-ice accretions (as will be considered herein).

In view of the absence of such detailed data, some previous data with 2-D protuberances on an airfoil are relevant. Jacobs[13] in 1932 tested a series of protuberances at different chordwise locations and varying heights on a NACA 0012 airfoil. The test revealed that the 5 and 15% chord locations on the airfoil upper surface were the most sensitive in terms of lift and drag penalties. In particular, this test showed dramatic reductions in lift, as much as 68% for a protuberance of k/c = 0.0125 (where k is the protuberance height and c is the airfoil chord length), and a large change in pitching moment. However, no locations between 5 and 15% were tested and the airfoil was not flapped. From analyzing the lift data of Jacobs,[13] Bragg[10,11] determined that the protuberances had caused a thin-airfoil stall and hypothesized that the same might be expected on an airfoil with spanwise-step ice. Recently, Calay, Holdo and Mayman[14] tested 3 different small (k/c = 0.0035) simulated runback ice shapes at 5, 15 and 25% chord on a low aspect-ratio NACA 0012 airfoil. The shapes at 5% had the largest effect on lift and drag, although the penalties were smaller than those seen by otherresearchers.

Wright and Potapczuk[15] presented recent results in computational modeling of the ice accretion and aerodynamic performance on airfoils in SLD conditions. Aerodynamic performance simulation was accomplished using a 2-D Navier-Stokes code with an algebraic turbulence model. The flow over three different airfoils was simulated with SLD shapes from tunnel measurements, LEWICE computational results, and the generic quarter-round shape. The ice accretion caused a large separation bubble which resulted in either a large leading edge separation or an early trailing-edge separation (which was often very unsteady at angles above 6°). Recently, Caruso and Farshchi[16] used an unstructured mesh flow code developed by Mavriplis[17] and demonstrated very high resolution of the detailed flowfield around a glaze-iced NACA 0012 airfoil. While neither of these studies examined the aerodynamic distributions and moments for airfoils with spanwise-step-ice accretions (as will be considered herein), they are of critical importance in paving the path for such predictions.

As such, knowledge of spanwise-step-ice accretions and their effect on airfoil and aircraft performance and control is still limited. This paper presents the initial findings of a comprehensive experimental and computational study of the aerodynamic effects of this type of simulated ice for k/c values of 0.0083 and 0.0139. The study examined the sensitivity of airfoil lift, drag, pitching moment and hinge moment to different chordwise locations, sizes and shapes of the ice simulation. The results may be applicable to other aircraft surfaces which contain simple flaps used for control. Future research will consider airfoil geometry effects, Reynolds number dependence and an attempt to gain a better understanding of the phenomena by a careful study of the fluid dynamics.

EXPERIMENTAL METHODOLOGY

Overview

The experimental tests were performed in the University of Illinois 3 × 4 foot Subsonic Wind Tunnel. An 18-inch chord modified NACA 23012 model with a 25% chord simple flap was used. The NACA 23012 airfoil was chosen because it has aerodynamic characteristics that are typical of the current commuter aircraft fleet. The detailed airfoil shape was generated through XFOIL by selecting the standard 23012 configuration. However,

XFOIL generates thicknesses on a vertical plane instead of normal to the mean camber line, producing a small difference near the leading edge as compared to a conventionally defined 23012. The result was a slightly drooped leading edge with a maximum vertical coordinate shift of 0.4% chord as compared to the conventional 23012. In addition, the maximum thickness of the airfoil model was 12.2%. As such, we will refer to the present airfoil as a NACA 23012m. However, it will be shown in the Experimental Validation section that the 23012m airfoil did not significantly alter the aerodynamic characteristics.

Figure 1 shows the schematic of the experimental setup. The leading edge of the flap was located at x/c = 0.75. The flap hinge line was located at x/c = 0.779. The model was attached to a three-component balance, which was also used to set the angle of attack. The flap was actuated by a two-arm linkage driven by a linear traverse system that was mounted on the metric force plate of the balance. A load cell was attached to one of the arms and measured the flap hinge moments. The model had 50 surface pressure taps on the main element and 30 surface pressure taps on the flap (including 12 spanwise taps). These were connected to an electronically scanned pressure (ESP) system. A traverseable wake rake with 59 probes was used to measure the drag. The wake rake pressures were also measured with the ESP system.

The lift coefficient (C_ℓ) and pitching moment coefficient (C_m) measurements were taken with the force balance and the surface pressure measurements. The primary drag coefficient (C_d) measurements were taken with the wake rake and confirmed with the force balance. The flap hinge moment coefficients (C_h) were measured with the flap hinge load cell and confirmed surface pressure measurements. The surface pressure measurements and florescent oil flow visualization were used to determine the location of separation bubbles and for flow diagnostics.

The spanwise step-ice accretions were simulated with wooden quarter round shapes. The shapes were taped to the surface of the model using 0.003 inch thick transparent tape. For selected cases, the boundary layer was tripped at x/c = 0.05 on both the upper and lower surfaces with 0.012 inch diameter microbeads which were applied onto a 0.003 inch thick and 0.25 inch wide double-sided tape.

Data Reduction

The C_ℓ, C_m, and C_d from the pressure and force balance measurements were calculated using standard methods with conventional definitions, e.g. the C_m was defined about the quarter chord and the C_h was obtained by determining the (trailing edge down) moment about the flap shaft and non-dimensionalizing by the flap surface area and the flap chord length. All of the aerodynamic coefficients were corrected for wall effects using the method described by Rae and Pope[18].

Shown in Table 1 are the uncertainty estimates of the aerodynamic coefficients for a typical data point. The case shown is that of the clean model at $\alpha = 5°$ with zero flap deflection and Re = 1.8 million. The relative uncertainties for C_m and C_h appear to be rather large, but this was due to relatively small reference values at this point.

Experimental Validation

The clean baseline measurements were taken and compared to previously published data in order to validate the experimental apparatus and data reduction methods in Fig. 2. The measurements were also compared to the results from XFOIL[19], an airfoil analysis code that uses an integral boundary element method. The present UIUC data was obtained at a Reynolds number (Re) of 1.8 million. Figure 2a shows the lift curve comparisons, which indicate good agreement between the present UIUC experiment and Stuttgart data[20] (taken at Re=2 million). The data of Abbott and von Doenhoff[21] showed a $C_{\ell max}$ that was approximately 8 percent higher which may have been due to their higher Reynolds number (Re=3 million). All of the experimental data showed leading-edge stall, as expected for the NACA 23012 airfoil. XFOIL, which was not designed to predict large separated flow regions, showed a more gradual stall and a higher $C_{\ell max}$.

Figure 2a shows that end wall effects were not significant as there was good agreement between the pressure data (which measured lift only near the model mid-chord) and the balance data (which measured the lift over the entire model). Had there been a significant wall induced 3-D effect, the pressure and the balance data would have differed by a greater amount. This consistency was also verified by flow visualization, which showed that significant 3-D flow was not present until past stall. This is in agreement with the significant difference in the pressure and balance data only after stall at $\alpha = 17°$.

Figure 2b shows the drag comparisons. It shows slightly higher drag values for the UIUC data which may have been due to the flap gap discontinuity and leakage. Figure 2c shows reasonable pitching moment comparisons, where the slightly higher values for the UIUC data are attributed to flap leakage. No previous experimental results were found for flap hinge moment comparisons. Also, XFOIL can not handle multi-elements and typically loses accuracy when predicting the thick boundary layer near the trailing edge; therefore it was not used to generate a C_h . Thus, Fig. 2d shows only the comparison between the UIUC pressure and flap hinge balance data that agreed reasonably well.

Figure 3 shows the comparison between the experimental surface pressures and those predicted by XFOIL. The angles of attack for the experimental data and XFOIL were 5.18° and 4.73°, respectively. This was done in order to match C_ℓ because XFOIL overpredicted lift, as shown in Fig. 2a. The resulting XFOIL C_P values were offset from the experimental results by a difference of about 0.05. However, they both followed very similar trends, including a laminar separation bubble at the upper surface that reattached at x/c = 0.20.

COMPUTATIONAL METHODOLOGY

Unstructured-Grid Navier-Stokes Code

A structured grid methodology, e.g. C-grid, has been found to be convenient for non-iced attached-flow single-element airfoils. However, many complex geometries, such as ice-accreted or multi-element airfoils, are not easily mapped onto such conventional structured grids. Furthermore, if there are protuberances that yield significant separation regions, it is often difficult to provide the high degree of resolution in the highly viscous shear regions away from the airfoil's immediate surface. One option to efficiently handle complex geometries and separation regions is to use unstructured grids. Such grids are typically made up of triangular elements, which can readily adapt to surface variations and through adaptivity to the local flow gradients. The code NSU2D (Navier-Stokes Unstructured 2-D) of Ref. 17 was designed for treating multi-element high-lift airfoils with complex shapes. The code was applied for a non-iced three-element airfoil by Valarezo and Mavriplis[22] where experimental surface pressure and lift at high angle of attack were well reproduced.

The NSU2D code employs a Galerkin-based finite element discretization of the full compressible Reynold's Averaged Navier-Stokes equations (without a thin layer assumption). Second and fourth order dissipation is applied for artificial dissipation to insure numerical stability. The code is being used herein to compute steady-state converged conditions. The convergence was accelerated by employing local time stepping and an algebraic multigrid algorithm (AMG) which employs subsets of the finest grid to automatically generate the coarse grids. In addition, the unstructured grid methodology of NSU2D can adapt to multi-element airfoils (Ref. 20), complex ice-shapes (Ref. 16), and regions of high flowfield gradients (Ref. 17) and thus may provide the high resolution necessary in regions of separated flow to make accurate predictions for the spanwise-step ice accretions considered herein.

The code supports both laminar flow and turbulent flow (using the Spalart-Allmaras model[23]) although the transition point must be user specified (Ref. 17). The clean-airfoil transition point is herein predicted *a priori* using the integral boundary-layer method program of XFOIL (Ref. 19) which incorporates a e^n criteria for transition. To account for variations in the predicted lift of XFOIL, a lift-corrected angle-of-attack is used when transition point is being computed. For the cases with a boundary-layer trip placed on the airfoil, the transition is assumed to occur at which ever comes first: the trip location or the transition location predicted by XFOIL.

The computations were completed on both the AAE Department SGI workstations and the NCSA (National Center for Supercomputing Applications) SGI Power Challenge Array. For the non-iced validation computations, a typical steady-state computation took about 2 hours of CPU using about 45,000 nodes and 400 multigrid cycles for convergence. The computations for the airfoils with the ice shape were more intensive and typically required 13 hours of CPU using a maximum of 120,000 nodes and 1000 multigrid cycles for convergence on the original (non-adapted) grid followed by 400 more multigrid cycles on the adapted grid.

Validations for Non-Iced Airfoils

Prior to its use with the present set of experimental data, the code was validated for previous experimental sets of non-iced cases (NACA 0012 and 23012 airfoils) in order to determine grid sensitivity/optimization and prediction robustness. The 0012 airfoil is valuable as a standard because of the availability of both experimental and computational data for the clean and iced airfoil shapes. The 23012 airfoil is also considered as it is relevant to the subject of the present experimental investigations.

For the NACA 0012 comparisons, the predictions obtained from NSU2D are first compared with the experimental data of Harris[24]. This data was chosen because of its accepted reliability[25] and due to the abundance of other CFD validations that have used the data[26]. The data was collected for a Mach number of 0.3 and a Reynolds number of three million with a transition trip placed at the 5% chord location on the upper and lower surfaces. The experimental data has been corrected using the linear method for simulating wall interference provided by Harris.

For these simulations, the computational domain was a square region, 40x40 chords, with the airfoil in the center and no tunnel walls. The high resolution grid contains 92,120 triangular elements, with 623 nodes on the airfoil surface and 49 nodes on the outer boundary. In the direction normal to the airfoil surface, there are approximately 50 nodes within the boundary layer with the first node approximately at a y/c of 2×10^{-6} and a 15% successive increase in grid size away from the wall.

Figure 4a shows the normal force coefficient (C_n) as a function of angle of attack for both the experimental data of Harris and the present computational methodology. The computational results are reported for only those angles which allowed convergence. Typically, the maximum converged angles correlated with the maximum lift conditions. The computational results from this and all other cases are in good agreement with the Harris data up to the maximum lift point. The results for normal force vs. drag coefficient also compare reasonably well (Fig. 4b). The results at the lower angles of attack match the experimental data within a few percent, but the code somewhat underpredicts the drag at the higher angles of attack. Some of this error can be attributed to the difficulties associated with selecting a transition location once transition moves forward of the transition trip. The code also appears to accurately predict the moment coefficient, C_m (Fig. 4c).

Plots of the pressure coefficient along the airfoil surface are shown for two angles of attack: 4.97° (Fig. 5a) and 11.90° (Fig. 5b). For both angles, the code was able to accurately reproduce the airfoil surface pressure fields, including the pressure spike at the airfoil's leading edge. Detailed grid resolution studies were conducted to note effects of various grid generation parameters and determine values required for accurate resolution. Studies where the number of nodes was increased by four-fold yielded less than 2% change in the lift, drag or any part of the pressure distribution. Therefore, the solution is considered reasonably grid independent.

The second set of validation calculations on the NACA 0012 were intended to asses the ability of the code to predict chord Reynolds number (Re) and freestream Mach number (M) effects by using the data of Ladson[27]. To see the effects of Reynolds number, the results for fixed Mach numbers of 0.15 and 0.30 for all Reynolds numbers considered are given in Figs. 6a and 6b, respectively. In both cases, we see that the code is able to predict the slight increases in both lift curve slope and maximum lift for increases in Reynolds number. However, in all cases there is a slight overprediction of the lift especially at the lower Mach number. Comparison of the two figures for constant Mach number conditions reveals that the computations successfully predict the slight increase in slope and the significant decrease in maximum lift for an increase in Mach number. Figure 7 directly illustrates these effects of Mach number for the intermediate Reynolds number case of $Re=4x10^6$. Therefore, the code is generally able to robustly predict trends due to both Mach number and Reynolds numbers variations on the lift curve slope and maximum lift for the non-iced 0012 airfoil. It is also worth noting that the code's accuracy improves for the higher Reynolds numbers and Mach numbers studied.

Validation of the code was also investigated for the NACA 23012 airfoil data set of Stuttgarter Profilkatalog I (Ref. 20). The measurements give the lift coefficient as a function of the angle of attack and the drag coefficient, over a range of Reynolds numbers. Computational setups similar to those used for the above NACA 0012 cases were used. Figure 8 shows lift and drag comparisons, at angles of attack ranging from -4 to 16.25 degrees, with a Mach number of 0.129 and a Reynolds number of 1.5 million. Figure 8a shows that NSU2D provides reasonable agreement but slightly overpredicts the lift curve slope, which may in part be due to inaccuracies in the XFOIL predicted transition point since no boundary layer trip was used in these experiments. The angle of attack at maximum lift was also predicted. It is worth noting that lift curve results at higher Reynolds numbers showed improved fidelity consistent with the above findings for the Ladson data. The relation between the lift and drag coefficients shown if Fig. 8b indicates NSU2D provides generally good predictions of the Stuttgart experimental drag measurements. Thus, the code is able to reasonably characterize the aerodynamic features up to the point of maximum lift for the non-iced NACA 23012 airfoil.

Methodology for Iced-Airfoils

The presence of the quarter-round ice shape on the airfoil required additional consideration computationally. The protuberance can cause a large separation bubble which will initiate at the top of the shape due to its sharp corner. This eliminates the problem with predicting the separation point of the free shear layer, which can be difficult to accurately simulate using RANS methodologies. For entrainment along the free shear layer itself, the flow can be considered fully developed turbulent in much less than one step height downstream of the separation point for the chord Reynolds numbers considered herein[28]. Therefore, the entire free shear layer is modeled as turbulent according to the Spallart-Allmaras model (Ref. 23). The reattachment region is also based on this model which slowly converges to a wall-bounded model as the flow becomes closer to the airfoil surface.

Figure 9a shows a closeup of the initial grid generated by NSU2D near the ice shape. This grid was deemed insufficient with respect to resolution of the resulting free shear layer. Therefore, grid adaptivity was employed using the technique similar to that of Mavriplis (Ref. 17). However, the present methodology based refinement on a flow variable gradient in a particular triangle whereas Mavriplis based it on the gradient along an edge. The present adaptation technique essentially subdivides any element for which gradients in the chosen parameter exceed a certain tolerance level. In addition, the present computations included a modification to allow interpolation of the converged original-grid flowfield results onto the adapted-grid domain for further computation. Figure 9b shows the grid resulting from one adaptation based on pressure gradients followed by a successive adaptation based on Mach number gradients. Figure 9c shows the corresponding Mach number contours for the initial converged solution for this angle. Note that additional grid points have been clustered around the separation point and along the high velocity gradients of the downstream free shear layer. It should be noted that additional refinement caused the solution to be less likely to converge. This is probably due to Kelvin-Helmholtz instabilities of the free shear layer[29] and/or separation bubble instabilities[30] which may overwhelm the turbulent viscosity once grid-size-dissipation is sufficiently reduced.

In addition to grid adaptation near the surface, it was also desired to employ a grid which formally included tunnel wall effects. Therefore, the present iced airfoil predictions are based on the upper and lower tunnel walls directly modeled within the computation by assuming slip (Euler) boundary conditions at these surfaces. To validate this approach for NSU2D, several simulations were conducted to compare the predictions using tunnel walls directly (then subsequently theoretically corrected a *posteriori* to an infinite domain) with the predictions using far-field free boundary conditions. In general, there were insignificant differences (e.g. less than 1%) between these two methods for prediction of the lift and drag as a function of angle of attack. For the moment coefficients, differences

on the order of those noted in Fig. 2c (e.g. deviations up to 0.02) were noted when comparing the corrected wall prediction with the free outer-boundary condition. All the iced-airfoil computations presented in the results section will include wall effects directly but theoretically corrected to remove the influence of the walls.

EXPERIMENTAL RESULTS

In this section, the C_ℓ and C_m data come from the integrated surface pressures and the C_d measurements were taken from the wake pressure data. The C_h data were taken from the flap hinge balance measurements. The integrated aerodynamic coefficient values will be presented first. They will be followed by the flowfield analysis which will help explain the integrated values.

Effect of Simulated Ice Ridge Location

The effect of ice shape location and size on the modified NACA 23012 aerodynamics will be discussed first. Figure 10 shows the effect of the 0.25" (k/c=0.0139) forward facing quarter round at three different x/c locations on aerodynamic coefficients. The boundary layer was tripped at 5% chord for the cases with the ice shapes at x/c = 0.10 and x/c = 0.20 and for the non-iced case. Figure 10a shows the lift curves with the ice shape at three different x/c locations. All of the iced cases showed reduced lift curve slopes (when compared to the clean case) even in the linear regions. The iced cases became nonlinear near $\alpha = 0°$ and also exhibited gradual stall characteristics as the lift coefficients leveled off near $C_{\ell max}$. The ice shapes dramatically reduced the $C_{\ell max}$, with the worst case being 0.3 for x/c = 0.10. The $C_{\ell max}$ increased to 0.56 when the ice shape was move upstream to x/c=0.02 and to 0.42 when it was moved downstream to x/c=0.20. The x/c=0.10 case had $\alpha_{stall}=6°$, which was the worst of the three iced cases.

Figure 10b shows the drag polars with the 0.25" ice shape at the three different x/c locations. It shows significant increases in drag when the ice shapes were attached to the model. The largest increase in drag occurred for $\alpha=0°$ when the ice shape was at x/c = 0.10, which also corresponds to the case with the lowest $C_{\ell max}$.

The pitching moments with the three ice shape locations are shown in Fig 10c. When the ice shape was at x/c=0.20, the pitching moment rapidly diverged from the non-iced case at $\alpha=-5°$, becoming more negative, indicating that the airfoil became more aft loaded. This occurred at $\alpha=0°$ with the ice shape at x/c=0.10. When the ice shape was located at x/c=0.02, the pitching moment diverged at $\alpha=2°$, but became more positive or front loaded. This continued until $\alpha=5°$, where it rapidly became more negative.

Figure 10d shows the flap hinge moments with the ice shapes at three different x/c locations. Between $\alpha=-9°$ and $\alpha=1°$, the hinge moments with the ice shape present were higher than that of the non-iced case. For positive angles of attack, the case with the ice shape at x/c=0.10 diverged from the clean case earliest at $\alpha=3°$. This again corresponded to the case with the lowest $C_{\ell max}$. The case with the ice shape at x/c=0.20 diverged from the non-iced case at the highest angle of attack (at 8°).

Effect of Simulated Ice Ridge Size

Figure 11 shows the effect of quarter round height on the modified NACA 23012 aerodynamics. Some of the figures to be presented will include predicted values as well, which will be described in the Computational Results section. The results are for the 0.15" and 0.25" forward facing quarter rounds placed at x/c=0.10 and $Re=1.8x10^6$. For the iced airfoil cases *and* the non-iced airfoil case, a boundary-layer trip was placed at the x/c=0.05 location.

Figure 11a shows that reducing the ice shape height from 0.25" to 0.15" increased the derivative of the lift coefficient to flap deflection ($C_{\ell,max}$) from 0.32 to 0.45 and increased α_{stall} from 6° to 8°. The drag comparisons between the two ice shape sizes are shown in Fig. 11b. As expected, the case with 0.25" ice shape had higher drag than the case with the 0.15" ice shape. The drag with the 0.15" ice shape exhibited a large break in the slope at $C_\ell=0.25$ while the drag with the 0.25" ice shape exhibited this break earlier at $C_\ell=0$.

Figure 11c shows the pitching moment comparisons. Decreasing the ice shape size to 0.15" delayed the onset of rapid divergence from the non-iced case from $\alpha=-1°$ to $\alpha=1°$. The flap hinge moment comparisons are shown in Fig. 11d. At negative angles of attack, the hinge moment with the 0.25" ice was more positive than the case with 0.15" ice. The 0.15" ice shape delayed the sudden break in the C_h slope until $\alpha=4°$. The hinge moments with the two ice shapes, however, merged at $\alpha=7°$.

Figure 12 shows the summary of $C_{\ell max}$ for the two ice shapes tested. The lowest $C_{\ell max}$ for the 0.25" ice occurred at x/c=0.12. The lowest $C_{\ell max}$ for the 0.15" ice occurred at x/c=0.10. The $C_{\ell max}$ for the 0.15" cases were higher than that for the 0.25" case at all x/c locations. However, they both followed the same general trends, with the minimum near x/c=0.10. Thus, it is clear from the Fig. 12 that in terms of lift loss, the most critical location for the ice shape of these size is near x/c = 0.10.

Effect on Flap Effectiveness

Tests were also conducted to determine the effect of the quarter round ice shape on flap effectiveness. Figure 13 shows the effect of quarter round location on C_ℓ as a function of flap deflection. The data shown are for the angle of attack fixed at 3°. For the zero flap deflection case, this was where the lift was non-linear but not yet stalled (as seen in Fig. 10a). The C_ℓ for the non-iced case was linear from $\delta_f= -10°$ to 5°. The non-linearity at higher flap deflection was probably caused by boundary-layer

separation over the flap. The trends at $\delta_f > 0$ are similar to that of Fig. 10a. The non-iced airfoil had the highest C_{ℓ}, followed by x/c=0.02, 0.20, and 0.10. The presence of the quarter round also decreased $C_{\ell\ \delta f}$. The slope (in the linear range) for the non-iced case was 0.0363/°, while that of the x/c=0.02, x/c=0.10, and x/c=0.20 cases were 0.0337/°, 0.0238/°, and 0.0279/° respectively. Again, it was the x/c=0.10 case which showed the greatest degradation in flapeffectiveness.

The effect of flap deflections on flap hinge moments as a function of angle of attack is shown in Fig. 14 for the 0.25" ice shape at x/c=0.10. The C_h curves for the various flap deflections are very similar, with approximately a 0.03 offset in C_h for every 5° flap deflection. However, increasing the flap deflection did cause the sharp break in the slope to occur earlier. At δ_f=-5°, this break occurred at α=2°, and at δ_f=10°, it occurred at α=0°.

Flowfield Analysis

Flowfield results will be discussed in this section in order to help explain the results of the preceding sections. Figure 15 shows a schematic of the generic flowfield around a forward facing quarter round. The boundary layer upstream of the quarter round separates at point A. The main flow recirculation ahead of the ice shape separates at point B. Point E is the reattachment zone of the primary separation bubble aft the ice shape.

Figures 16a and 16b show the florescent oil flow visualization image and the surface pressure coefficients for the case with the 0.25" forward facing quarter round at x/c=0.10. The Reynolds number was 1.8 million and the angle of attack was 3°. The boundary-layer trip was not used for this case. The bright spots on the picture indicate the presence of oil, where the horizontal streaks are regions where the oil is flowing. The vertical line (which indicated pooling of oil) at x/c=0.05 was where the boundary layer separated ahead of the ice shape and corresponds to point A in Fig. 15. The second vertical line at x/c = 0.07 was the separation point of the recirculation zone ahead of the ice shape and corresponds to point B in Fig. 15. The quarter round is located between points C and D. The region between D and E was the main separation bubble aft of the quarter round. The reattachment zone E (located between the two E's shown) was characterized by fine, scattered beads and was not clearly defined. This was thought to be the result of unsteady reattachment. The vertical line at x/c=0.77 was the oil pooling on the flap gap.

Most of the features discussed above can be seen in the surface pressure plot shown in Fig. 16b. The C_P decreased from 1 at the leading edge to 0 at x/c=0.05, where it started to increase again. This local minimum in C_P was where the boundary layer separated upstream of the ice shape. The pressures increased from x/c=0.05 to x/c=0.10. The C_P then dropped sharply to -1 and then leveled off. This indicated that the flow had separated immediately downstream of the quarter round. The C_P approached the clean model values near x/c=0.70 where the boundary layer reattached. The pressure at the trailing edge with the ice shape present was lower than the clean case. This was expected since there was less pressure recovery and an increase in drag due to the ice shape. The pressures in the quarter round case also seemed to be offset from the baseline case. This is a feature typically observed when the airfoil is thickened. Thus, it appeared that the ice shape effectively thickened the airfoil by the addition of the separation bubble.

Figure 17 shows the summary of the boundary-layer state observed from the florescent oil flow visualization. It shows that the primary forward separation bubble started at x/c=0.07 at α=0°. This location moved gradually upstream to x/c=0.05 at α=3° and remained stationary to α=5°. The secondary separation bubble upstream of the quarter round (as depicted in Fig. 15) is not shown because it was not clearly defined and could not be accurately resolved. The primary downstream bubble reattachment zone was located between x/c=0.40 and x/c=0.44 at α=0°. This zone moved downstream as α was increased. At α=3.25°, this zone was located between x/ =0.75 and the trailing edge. Thus, for 0.25" quarter round at x/c=0.10, the stall was initiated by a rapidly growing separation bubble that eventually reached the trailing edge, which is characteristic of a thin airfoil stall. There was no evidence from flow visualization of a trailing edge separation.

Figure 18 shows the surface pressure coefficients with the 0.25" quarter round at 3 x/c locations and at α=3°. When the quarter round was placed at x/c=0.02, the aft separation bubble reattached at x/c=0.15, resulting in a separation bubble that covers 13% of the chord. When the quarter round was at x/c = 0.10, the aft bubble reattached at x/c = 0.70, with the bubble covering 60% of the chord. When the quarter round was placed at x/c = 0.20, the bubble reattached at x/c = 0.80, resulting in a bubble that covered 60% of the chord. Thus, the effect of the ice shape at x/c = 0.02 was not as severe as the effect at x/c = 0.10 or x/c = 0.20 (as evident in Fig. 10a) because the separation bubble was not as large. This was probably due to the favorable pressure gradient present at the quarter round location which assisted the reattachment process. The effect of the ice shape at x/c = 0.20 was not as severe as the effect at x/c = 0.10 because the quarter round was downstream far enough that a negative pressure spike was able to form between the leading edge and x/c = 0.18. This was not present in x/c = 0.10 case.

The pressures near x/c = 0.10 with the quarter round at x/c = 0.02 were even lower than the clean case. This may have been due to the flow accelerating over the quarter round and resulted in a lift distribution that was more front loaded. It is also evident from Fig. 18 that the cases with the quarter round at x/c = 0.10 and x/c = 0.20 resulted in more aft loaded lift distributions. The effect of this is clearly shown in the pitching moments plots in Fig. 10c. It shows that C_m at α = 3° for the x/c = 0.02 case was higher than the non-iced case while C_m's for the x/c = 0.10 and 0.20 cases were significantly lower.

COMPUTATIONAL RESULTS

In the following section, the aerodynamic influence of the ice shape will be considered computationally by varying its maximum height. In addition, a case with no ice shape which includes only the boundary layer trip will be used as a reference condition. As before, the code was run for all experimental angles but only conditions which were fully converged are reported on the figures.

Effect of Simulated Ice Ridge Size

The effect on the lift curve of a 0.15" (k/c=0.0083) and a 0.25" (k/c=0.0139) ice shape located at x/c=0.1 is shown in Fig. 11a for both the present experiments and present computations (with M=0.2 and Re=1.8×10^6). It should be noted that the present results employed the adaptive grid for the 0.15" ice shape but not for the 0.25" ice shape (since it was not yet available at the time of this paper). However, the difference is not expected to be very large for the 0.25" case based on the changes noted in the 0.15" case. In general, the NSU2D predictions for the no-ice shape compared reasonably well with the experimental results, although the slope of the lift curve and maximum C_ℓ are overestimated, similar to the predictions of the low Reynolds number cases in the computational validations. It should be recalled that the findings in the validation section noted the prediction accuracy was increased as Reynolds number increased. As such, we expect the predictions for higher Reynolds number conditions (consistent with actual flight conditions) to be improved.

The significant reduction in lift curve slope and the dramatic reductions in maximum C_ℓ and maximum-lift angle caused by the ice shape presence were predicted reasonably well by NSU2D. The qualitative performance of the code was very good in predicting decreased lift as the ice-shape height was increased. However, the NSU2D predictions exhibited a weaker break in the lift curve slope than that shown by the experiments. This is probably attributed to differences in the separation bubble behavior between the computations and the measurements, which will be discussed later. It should also be noted that the transition point for the iced airfoil was always taken as the trip location. This is because the iced case was limited to low lift coefficients such that the lift-corrected non-iced XFOIL transition was never further upstream than the trip location. However, computational NSU2D tests where the trip location was arbitrarily moved further upstream did not change the results significantly.

Figure 11b shows the C_ℓ vs. C_d results where the trends due to the presence and height-change of the ice-shape are well predicted by NSU2D. Considering the large amount of separation occurring for the iced airfoil flows, the performance of the simulations was quite encouraging. However, the iced airfoil computations were not able to converge for many of the negative angles-of-attack. This is perhaps a result of the instability of the separation bubble upstream of the ice-shape and/or its proximity to the primary stagnation point which is on the upper surface at these conditions. The slight underprediction of the drag coefficient at higher lift conditions of the non-iced case is consistent with the validation computations (e.g. Fig. 4b and 8b).

Figure 11c shows the pitching moment coefficient distribution with α, where NSU2D predicts the strong drop-off in moment at positive angles of attack as the ice shape increases in size. However, the computations do not predict the increase in moment coefficient for angles of seven degrees or more and the non-iced airfoil case shows deviations from experiment on the order of 0.02. The latter result was due to a combination of small differences in the pressure distribution both on the forward upper surface of the quarter chord and on the lower surface aft of the quarter chord, which are discussed later.

Perhaps the most import aerodynamic coefficient with respect to the airfoil control is that of the hinge moment. The comparison between computation and experiment of this sensitive parameter is shown in Fig. 11d. Again NSU2D successfully predicts the qualitative trends resulting from the presence and change in height of the ice shape. In particular the increased drop-off in C_h at high angles of attack is reproduced for angles of attack as high as eleven degrees.

The above results indicate that NSU2D robustly predicts the trends of the all the major aerodynamic features associated with the ice-shape presence for these experimental conditions. In addition, the quantitative comparison is reasonable for much of the present conditions. And as previously mentioned, the predictions for higher Reynolds number conditions (consistent with actual flight conditions) are expected to be improved.

Flowfield Analysis

Finally, we consider some of the aerodynamic details responsible for the integrated quantities discussed above. Figure 19 shows a comparison of the experimental and computational pressure distributions for the non-iced, 0.15", and 0.25" ice shape at a three degrees angle of attack. The non-iced pressure distribution shows an overprediction of the suction pressure on the forward upper surface and an overprediction of the aft lower surface pressure. This was mentioned earlier with respect to the deficiency of the moment coefficient predictions at high angles of attack of Fig. 11c. Since the non-iced aerodynamics of the NACA 23012 airfoil can be particularly sensitive to transition point location, the pressure distribution differences at high angles of attack may be attributed to the insufficient prediction of transition point given by XFOIL.

The predicted pressure distribution over the 0.15" ice shape conforms reasonably with the experimental data considering the large separated flow region on the upper surface (Fig. 19b). NSU2D gives excellent agreement along the lower surface and along the upper surface in front of the ice shape. The code reasonably predicts the pressure increase in the stagnation region ahead of the ice shape at

these conditions. Most of the error in the solution is located in the large separation region aft of the ice shape. Although NSU2D accurately predicts the magnitude of the suction peak occurring downstream of the ice shape, it displays a much faster pressure recovery than the experimental data. This error is thought to be partially due to the turbulence model inadequately predicting the amount of entrainment within the shear layer. It is also felt that additional grid refinement in this region might improve the solution. Similar comparisons with experiment are found for the predictions of the 0.25" ice shape case (Fig. 19c). Comparisons of the pressure distribution at higher angles for the both ice-shape cases revealed a similar level of discrepancy despite longer and thicker separation regions. This was attributed to the fact that the reattachment point had become fixed at the trailing edge for both the experiment and the computation (a reattachment condition more easily predicted).

Figure 20 plots some of the velocity vectors within the separation bubble for the 0.15" ice shape at α=0°. Note, if all the velocity vectors were plotted the figure would be too dense to be clear (recall mesh detail given in Fig. 9c). The velocity vector figure shows the large aft separation bubble extending from the top of the ice shape with an initial expansion upwards (which is thought to be the cause of the suction peak mentioned in the Fig. 19b and 19c descriptions). The small recirculation region upstream of the ice shape shows a vertical extent which is less than the top of the ice shape, a result which is consistent with the buff-body experiments of Winkler[31]. In addition, the lack of a clearly defined secondary recirculation bubble upstream of the ice shape is consistent with the Fig. 17 experimental results.

The predicted boundary-layer state is presented in Fig. 21 for comparison with the experimental counterpart (Fig. 17). Reattachment locations were determined by examining skin friction coefficients. In general, the computations predict later reattachment than the experimental flow visualization. This is surprising given the nature of the differences in the pressure recovery mentioned above. At α=2°, NSU2D predicts that the entire upper surface is separated, while the experiment does not predict this until after 3 degrees. It is worth noting that although the computational reattachment location is presented as a single point, experimental reattachment fluctuates over a significant region (as much as 0.2c in length).

The experimental observation of unsteady reattachment suggests that the separation bubble itself was unsteady, a feature which can not be captured with the current computational strategy. As such further improvements of the NSU2D prediction accuracy may be realized by using an unsteady simulation. Modification to the code to allow unsteady flow, along with examinations of the effect of ice shape location and flap deflection influence are subjects of current research for the computational portion of this ongoing project.

CONCLUSIONS

The experimental and computational investigation demonstrated dramatic changes on the sectional aerodynamic characteristics as a result of the presence of quarter-round spanwise ice shapes of heights of k/c=0.0083 and 0.0139. The measurements showed reduced lift curve slopes (as compared to the non-iced airfoil) followed by a gradual stall at relatively low angles of attack, e.g. six degrees. For no flap deflection, the resulting maximum lift coefficients were as low as 0.3 in the worst case (which corresponded to an x/c location of 0.12 and k/c=0.0139). The ice shapes were also observed to significantly degrade flap effectiveness even before stall. In addition, the airfoil moment and hinge moment coefficients were both significantly negative at positive angles of attack when the ice shape was present. Oil flow visualizations coupled with pressure distributions indicated a thin airfoil type of stall.

The NSU2D code was extensively validated with several non-iced airfoil experiments including effects of Reynolds number and Mach number. The computational results for the present iced-airfoil experiments indicate that NSU2D robustly predicts the trends of all the major aerodynamic features associated with the ice-shape presence. In addition, the quantitative comparisons of lift, drag and moments are reasonable for much of the current experimental conditions. In particular, NSU2D gave predictions of hinge moment which were well correlated with the experimental data in terms of both quantitative representation and qualitative trends for both the non-iced airfoil and the iced airfoils . This is important since prediction of the ice shape effect on hinge moment is critical to forecasting the possible influence of SLD on aileron or rudder control. Finally, the predictions for higher Reynolds number conditions (consistent with actual flight conditions) are expected to show higher fidelity based on the validation computations.

ACKNOWLEDGMENTS

This work was supported by the Federal Aviation Administration (FAA) under grant DTFA MB 96-6-023 with Dr. James Riley as technical monitor. The computations were all performed under NCSA grant CTS970036N. The authors would also like to gratefully acknowledge the assistance of Mr. Gene Hill , Mr. Tom Bond, Dr. Mark Potapczuk, and Dr. Dimitri Mavriplis.

REFERENCES

[1] Dow Sr., John P., "Roll Upset in Severe Icing," Federal Aviation Administration - Aircraft Certification Service, September 1995.

[2] National Transportation Safety Board, "Icing Tanker Test Factual Report," Docket No: SA-512, Exhibit No: 13B, DCA95MA001, Washington D.C., Feb. 16, 1995.

[3] Johnson, C.L., "Wing Loading, Icing and Associated Aspects of Modern Transport Design," *Journal of the Aeronautical Sciences,* vol. 8, no. 2, December 1940, pp. 43-54.

[4] Morris, D.E., "Design to Avoid Dangerous Behavior of an Aircraft Due to the Effects on Control Hinge Moments of Ice on the Leading Edge of the Fixed Surface," Aeronautical Research Council, Technical Note No. Aero. 1878, Current paper No. 66, London, March 1947.

[5] Thoren, R.L., "Icing Flight Tests on the Lockheed P2V," ASME paper no. 48-SA-41, 1948.

[6] Cooper, W.A., Sand, W.R., Politovich. M.K., and Veal, D.L., "Effect of Icing on Performance of a Research Airplane," *Journal of Aircraft,* Vol. 21, no. 9, September 1984, pp. 708-715.

[7] Ashenden, R. and Marwitz, J., "Turboprop Aircraft Performance Response To Various Environmental Conditions," AIAA Paper 97-0305, *Journal of Aircraft,* Vol 34, no. 3, May-June 1997, pp. 278-287.

[8] Ashenden, R., Lindberg, W. and Marwitz, J., "Two-Dimensional NACA 23012 Airfoil Performance Degradation by Super Cooled Cloud, Drizzle, and Rain Drop Icing," AIAA 34th Aerospace Sciences Meeting, Reno, NV, January 15-18, 1996.

[9] Trunov, O.K. and Ingelman-Sundberg, M., "On the Problem of Horizontal Tail Stall Due to Ice," Report JR-3, The Swedish Soviet Working Group on Scientific-Technical Cooperation in the Field of Flight Safety, 1985.

[10] Bragg, M.B., "Aircraft Aerodynamic Effects Due To Large Droplet Ice Accretions," Paper No. 96-0932, AIAA 34th Aerospace Sciences Meeting, Reno, NV, January 15-18, 1996.

[11] Bragg, M.B., "Aerodynamics of Supercooled-Large-Droplet Ice Accretion and the Effect on Aircraft Control," *Proceedings of the FAA International Conference on Aircraft Inflight Icing,* Volume II, DOT/FAA/AR-96/81,II, August 1996, pp. 387-399.

[12] Mullins, B. R., Smith, D. E., and Korkan, K. D., "Effect of Icing on the Aerodynamic Performance of a Flapped Airfoil," AIAA Paper 95-0449, Reno, Jan., 1995.

[13] Jacobs, E. N., "Airfoil Section Characteristics as Affected by Protuberances," NACA Report No. 446, 1932.

[14] Calay, R.K., Holdø, A.E. and Mayman, P., "Experimental Simulation of Runback Ice," *Journal of Aircraft,* Vol. 34, No, 2, March - April, 1997, pp. 206-212.

[15] Wright, W. B. and Potapczuk, M. G., "Computational Simulation of Large Droplet icing," *Proceedings of the FAA International Conference on Aircraft Inflight Icing,* Volume II, DOT/FAA/AR-96/81,II, August 1996, pp. 545 - 555.

[16] Caruso, S.C. and Farshchi, M. "Automatic Grid Generation for Iced Airfoil Flowfield Predictions" AIAA Paper 92-0415, Reno, NV, 1992.

[17] Mavriplis, D. "Multigrid Solution of Compressible Turbulent Flow on Unstructured Meshes using a Two-Equation Model" NASA Contractor Report 187513, NASA Langley Research Center, ICASE, January 1991.

[18] Rae, W. H. and Pope, A., *Low-Speed Wind Tunnel Testing,* John Wiley & Sons, 1984.

[19] Drela, M., "XFOIL 6.6 User Primer", MIT Aero & Astro Engineering, March 14, 1996.

[20] Althaus, D. and Wortmann, F. "Experimental Results from the Laminar Wind Tunnel of the Institute for Aerodynamic and Gasdynamics - The University of Stuttgart" published by Princeton University, Department of Mechanical and Aerospace Engineering, 1979.

[21] Abbott, I. H. and von Doenhoff, A.E., *Theroy of Wing Sections,* Dover Press, 1959.

[22] Valarezo, W. O. and Mavriplis, D. "Navier-Stokes Applications to High-Lift Airfoil Analysis" AIAA Paper 93-3534, Monterey, CA, 1993.

[23] Spallart, P.R. and S.R. Allmaras "A One-Equation Turbulence Model for Aerodynamic Flows", AIAA 30th Aerospace Sciences Meeting & Exhibit, AIAA-92-0439, January 1992.

[24] Harris, C.D., "Two-Dimensional Aerodynamic Characteristics of the NACA 0012 Airfoil in the Langley 8-Foot Transonic Pressure Tunnel", NASA TM 81927, 1981.

[25] McCroskey, W.J. "A Critical Assessment of Wind Tunnel Results for the NACA 0012 Airfoil", AGARD, Aerodynamics Data Accuracy & Qulaity: Requirements & Capabilities in Wind Tunnel Testing, July 1988.

[26] Holst, T.L. "Viscous Transonic Airfoil Workshop Compendium of Results" AIAA 19th Fluid Dynamics, Plasma Dynamics & Lasers Conference, AIAA-87-1460, June1987.

[27] Ladson, C.L. "Effects of Independent Variation of Mach and Reynolds Numbers on the Low-Speed Aerodynamic Characteristics of the NACA 0012 Airfoil Section", NASA TM 4074, 1988.

[28] Oakley, T., E. Loth, and R. Adrian "Cinematic Particle Image Velocimetry of a Turbulent Free Shear Layer ," *AIAA J.ournal* , Vol. 34, No. 2, pp. 299-308, February 1996.

[29] Oh, C. and E. Loth "Unstructured Grid Simulations of Spatially Evolving Supersonic Shear Layers," *AIAA J.ournal* Vol. 33, No. 7, pp. 1229-1238, July 1995.

[30] Loth, E. and M. Matthys "Unsteady Low Reynolds Number Shock Boundary Layer Interactions," *Physics of Fluids,* Vol. 7, No. 5, pp. 1142-1150, May 1995.

[31] Winkler, J. F. "Local Flowfield about Large Distributed Roughness Elements in a Laminar Boundary Layer" Ph.D. Thesis, University of Illinois at Urbana-Champaign, Urbana, IL, 1996.

TABLES AND FIGURES

Aerodynamic Coefficient	Reference Value	Absolute Uncertainty	Relative Uncertainty
C_l Balance	0.60993	1.87E-03	0.31%
C_d Balance	0.0125	1.96E-04	1.57%
C_m Balance	-0.0055	-2.13E-05	0.39%
C_h Balance	-0.0157	-3.55E-03	9.70%
C_l Pressure	0.633	2.11E-03	0.33%
C_d Pressure	0.01022	1.43E-04	1.40%
C_m Pressure	-0.00894	-3.49E-04	3.90%
C_h Pressure	-0.0186	-9.30E-04	5.00%

Table 1: Experimental uncertainties for the clean model at $\alpha = 5°$, $\delta_f = 0°$, $Re = 1.8x10^6$.

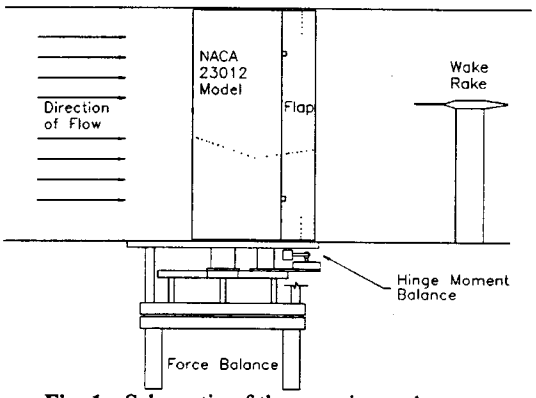

Fig. 1: Schematic of the experimental setup.

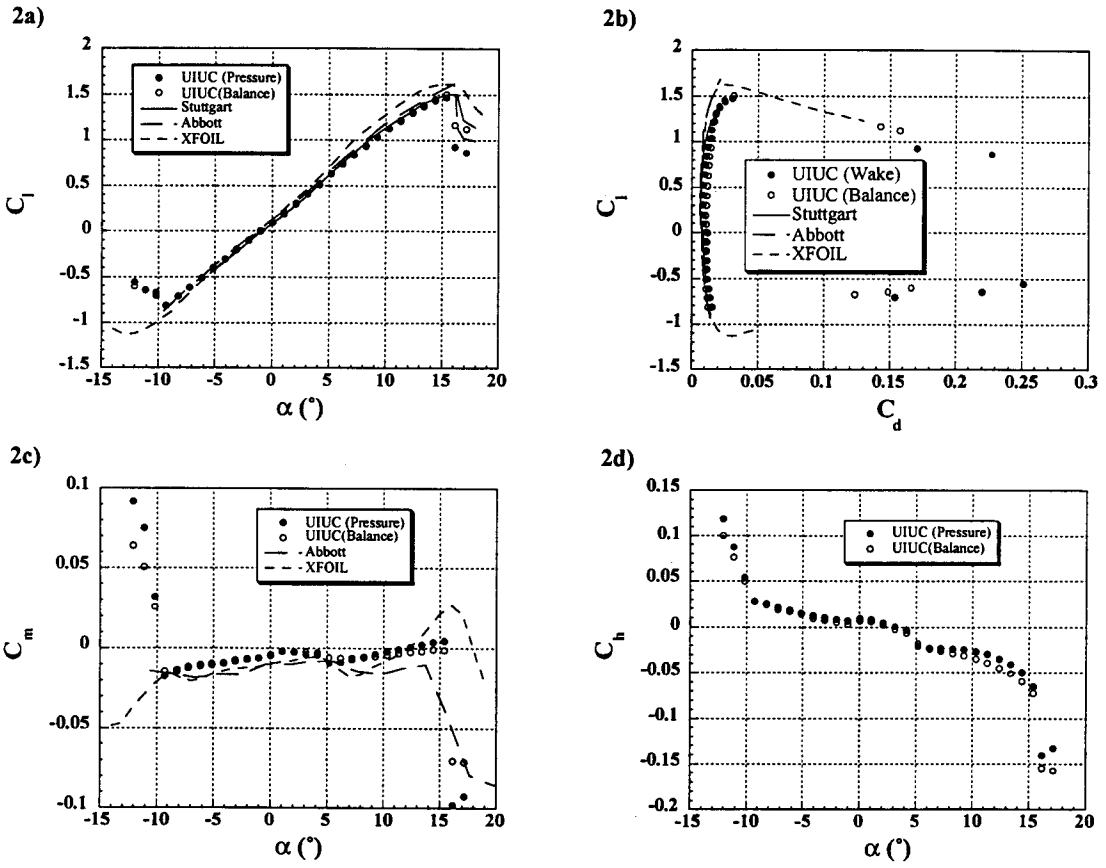

Fig. 2: Aerodynamic coefficients of clean model. Present data and XFOIL: NACA 23012m and $Re=1.8x10^6$; Abbott and von Doenhoff: NACA 23012 and $Re=3x10^6$; Stuttgart: NACA 23012 and $Re=2x10^6$.

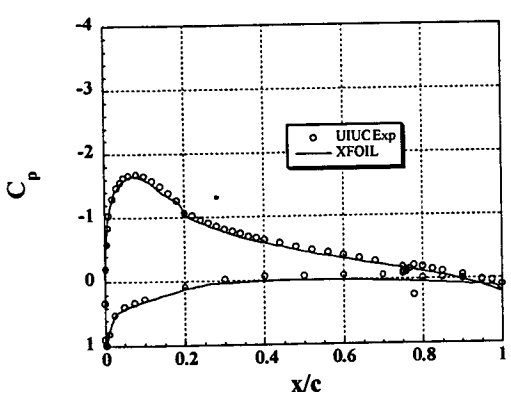

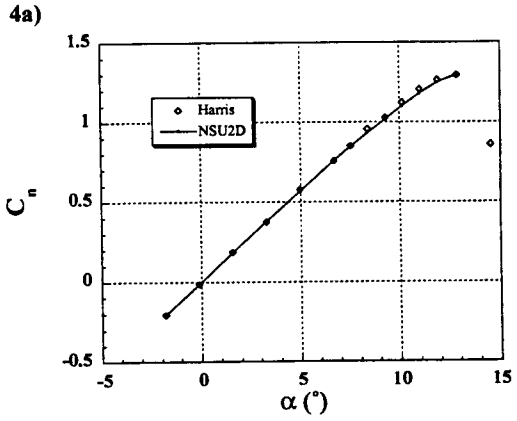

Fig. 3: Surface pressure on clean NACA 23012m model at Re=1.8x10^6. Experiment α=5.18°; XFOIL α=4.73°; C_ℓ=0.633.

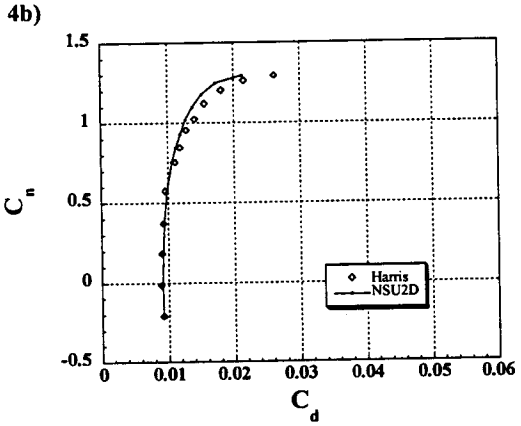

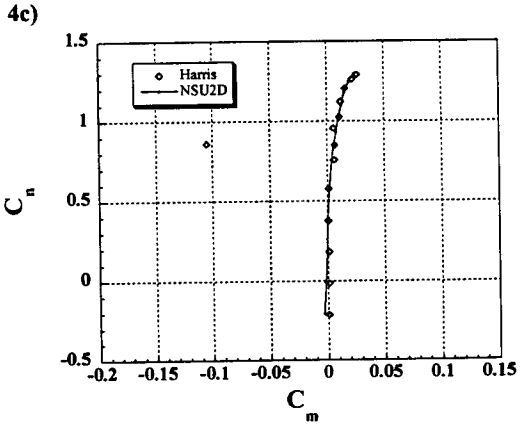

Fig. 4: Harris data and NSU2D predictions for NACA 0012 at Re=3x10^6 and M=0.3.

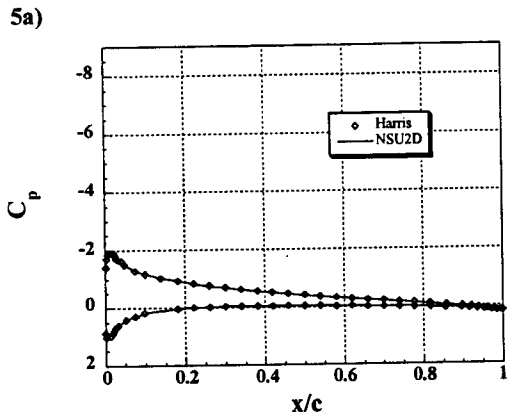

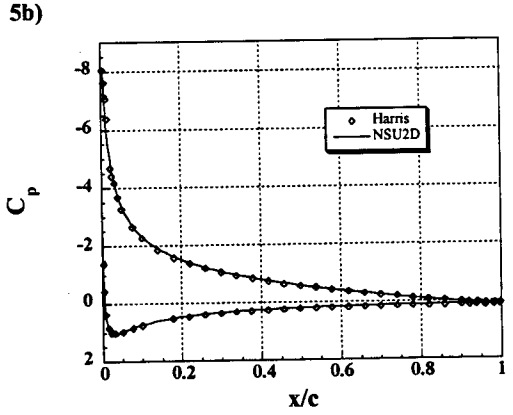

Fig. 5: Harris data and NSU2D prediction for NACA 0012 pressure coefficient distribution at a) α=4.9657° and b) α=11.9024°.

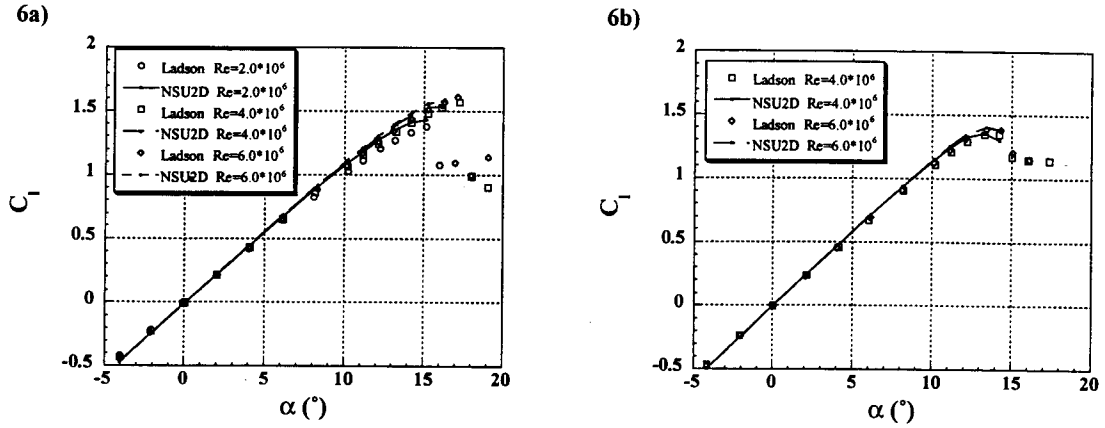

Fig. 6: Lift curve for Ladson and NSU2D predictions for NACA 0012 at Mach numbers of a) 0.15 and b) 0.30.

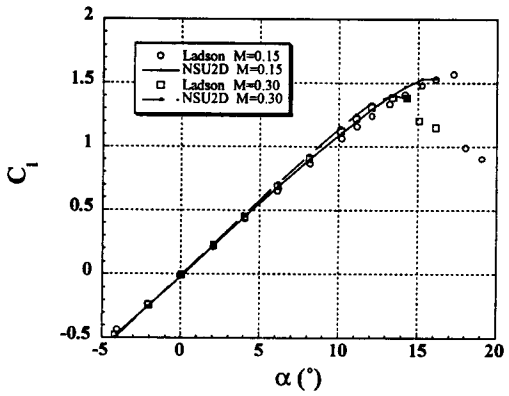

Fig. 7: Lift curve for Ladson and NSU2D predictions for NACA 0012 at Reynolds number of $4x10^6$.

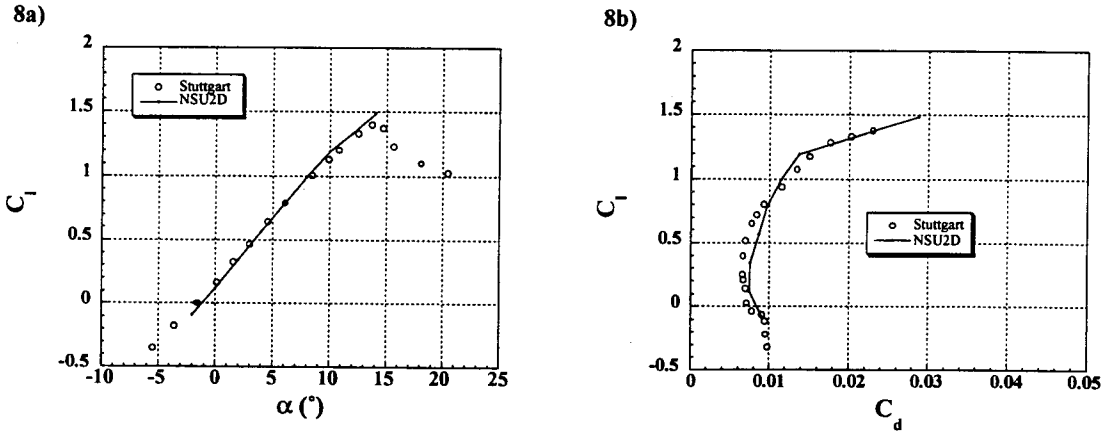

Fig. 8: Stuttgart data and NSU2D predictions for NACA 23012 at $Re=1.5x10^6$ and M=0.129.

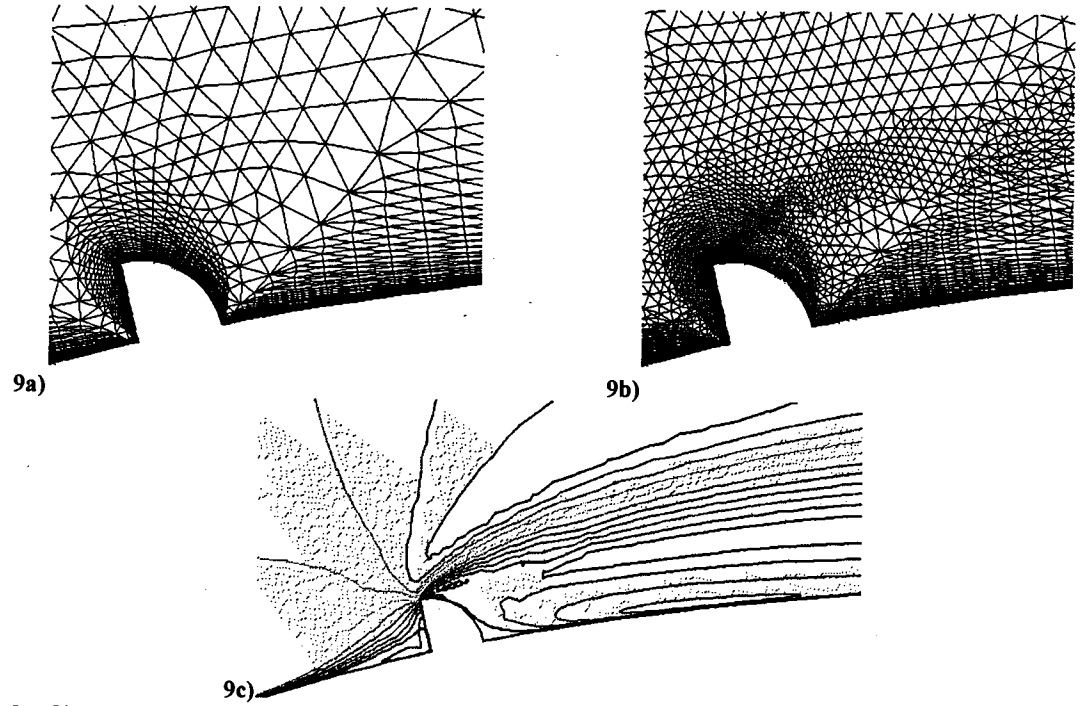

Fig. 9: Close up near 0.15" ice-shape of a) original grid, b) adapted grid, and c) mach number contours on original grid.

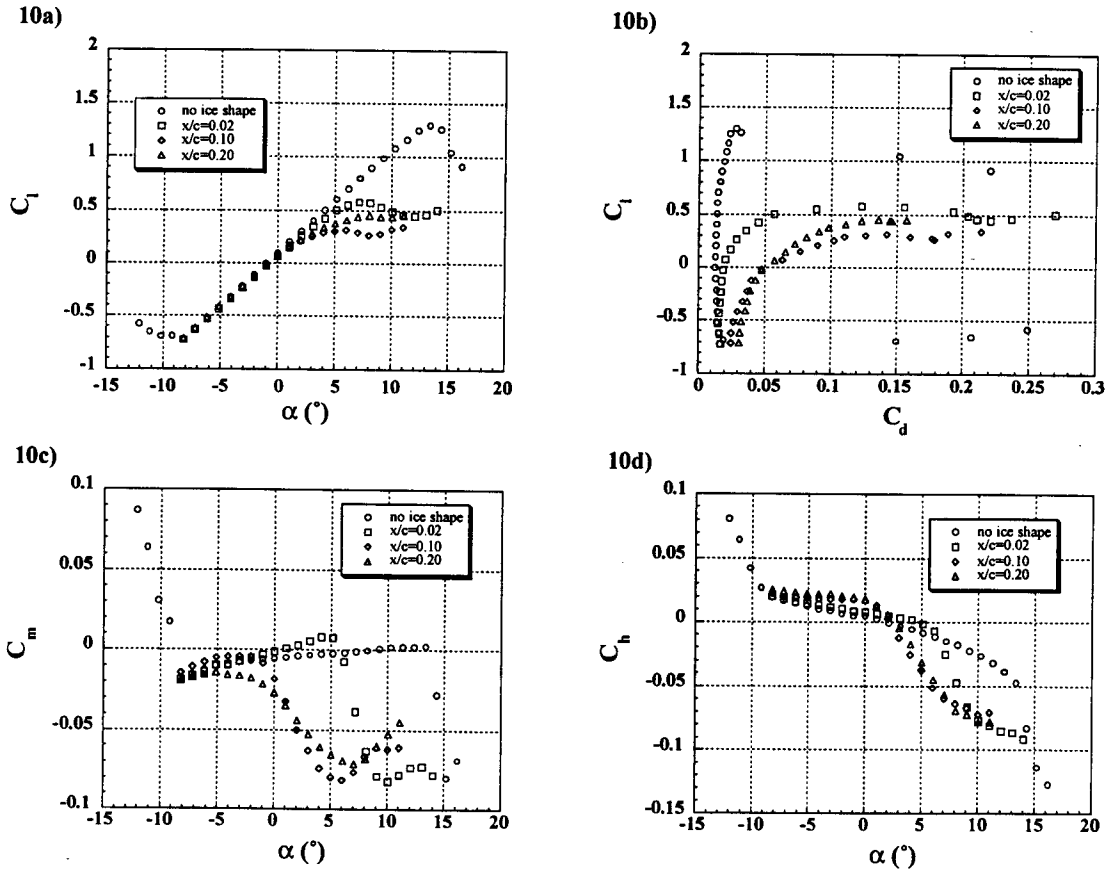

Fig. 10: Effects of 0.25" quarter round on aerodynamic coefficients for present experiments with NACA 23012m: B.L tripped at 5% chord for all cases except x/c=0.02; Re=1.8x10^6.

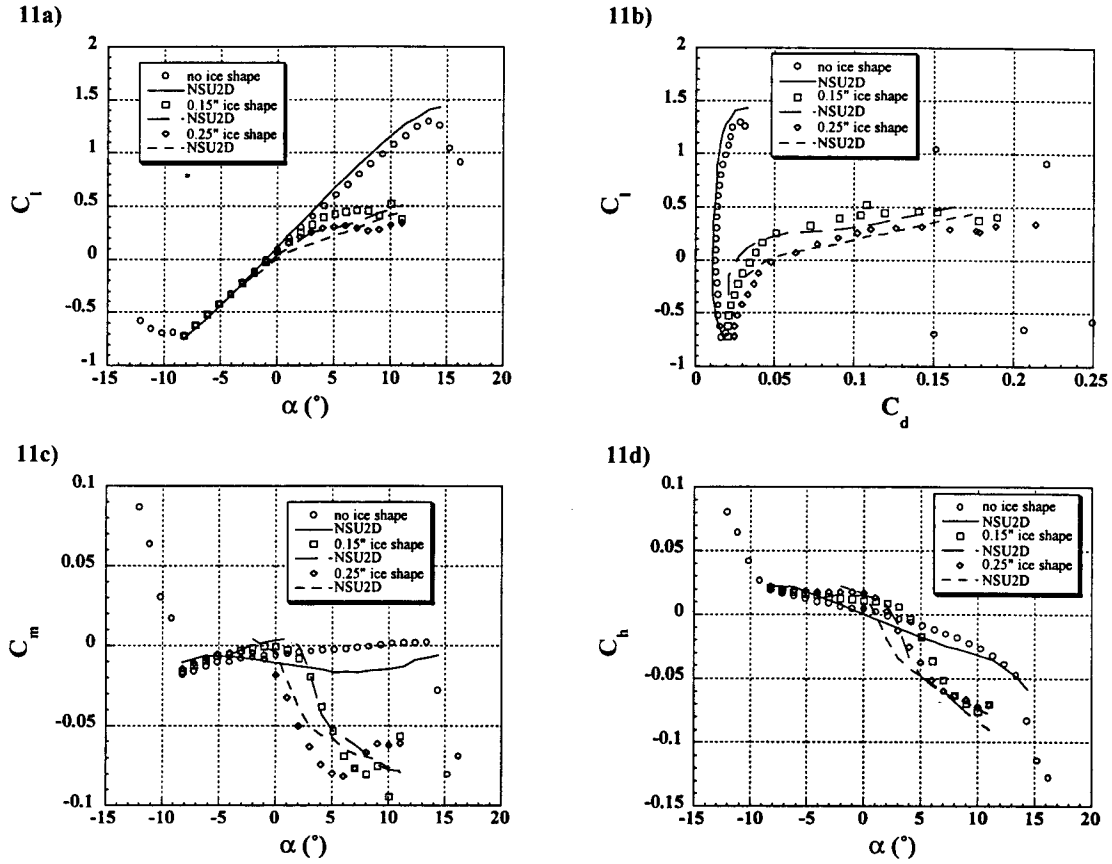

Fig. 11: Effect of quarter round height on aerodynamic coefficients for present experiments and NSU2D predictions with NACA 23012m: quarter round at x/c=0.10; B.L. tripped at 5% chord; $Re=1.8x10^6$.

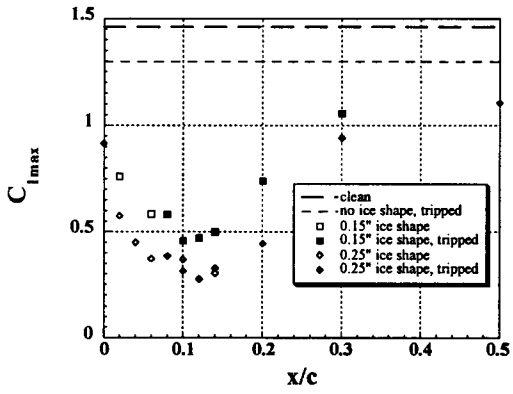

Fig. 12: Summary of C_{lmax} with quarter round at various x/c locations for present experiments with NACA 23012m.

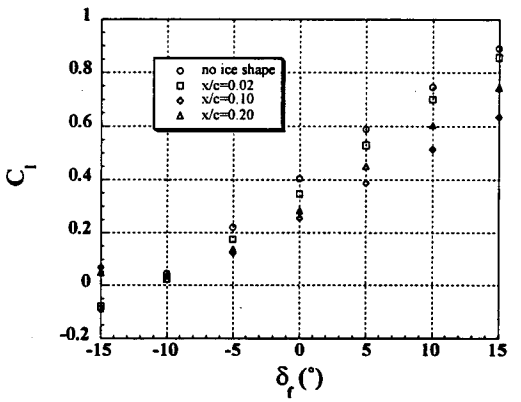

Fig. 13: Lift coefficient as a function of flap deflection for present experiments with NACA 23012m: 0.25" quarter round; α=3°; $Re=1.8x10^6$.

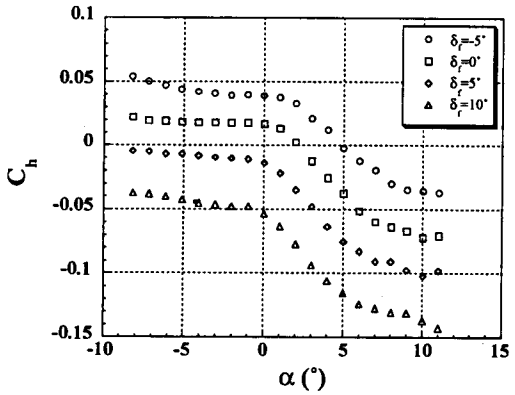

Fig. 14: Flap hinge moment coefficient with varying flap deflection for present experiments with NACA 23012m: 0.25" quarter round at x/c=0.10; Re=1.8x10^6.

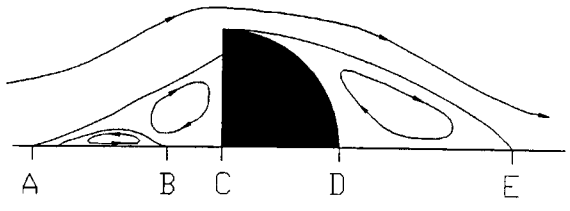

Fig. 15: Flowfield schematic about forward facing quarter round.

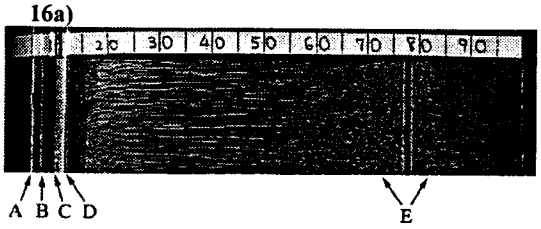

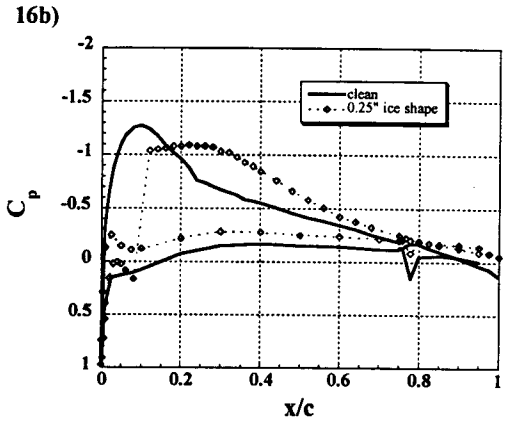

Fig. 16: Surface distributions for present experiments with NACA 23012m: 0.25" quarter round at x/c=0.10; B.L. not tripped; α=3° ; Re=1.8x10^6 for a) florescent oil flow visualization and b) pressure measurement.

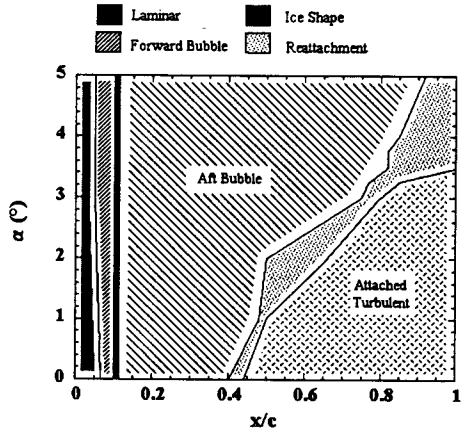

Fig. 17: Summary of experimental boundary-layer state with 0.25" quarter round at x/c=0.10 obtained from flow visualization. B.L. not tripped; Re=1.8x10^6.

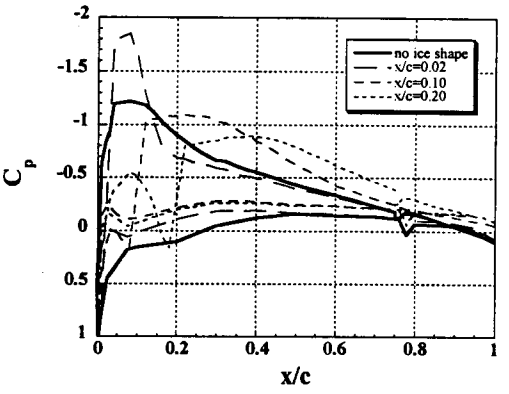

Fig. 18: Experimental surface pressures with 0.25" quarter round at 3 x/c locations. B.L. tripped at 5% chord except for x/c=0.02; α=3°; Re=1.8x10^6.

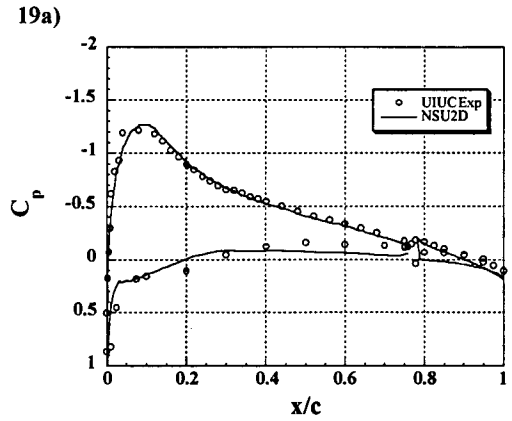

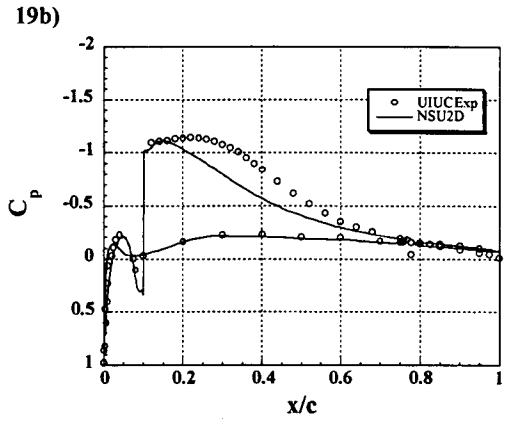

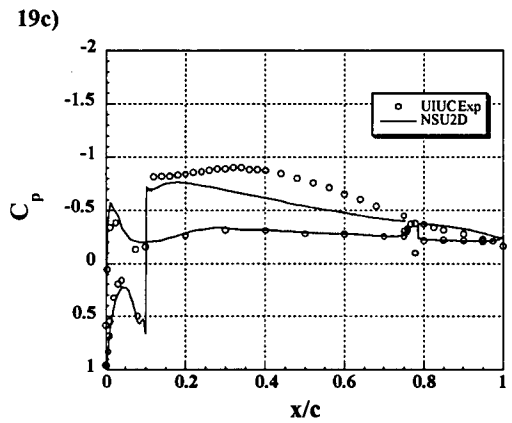

Fig. 19: Surface pressure distributions for present experiments and NSU2D predictions with NACA 23012m: quarter round at x/c=0.10; B.L. tripped at 5% chord; α=3°; Re=1.8x10^6. For a) no ice shape, b) 0.15" ice shape, and c) 0.25" ice shape.

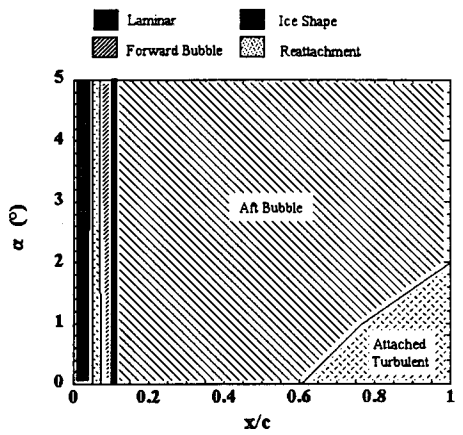

Fig. 21: Summary of computational boundary-layer state with 0.25" quarter round at x/c=0.10: B.L. tripped at 5% chord; Re=1.8x10^6.

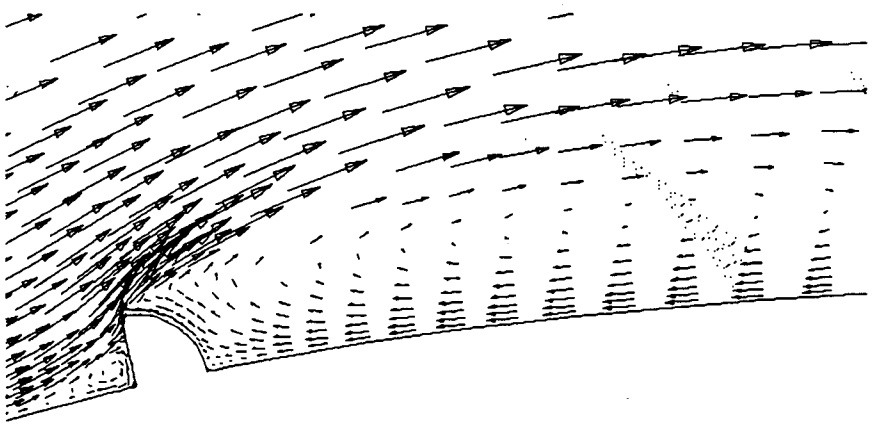

Fig. 20: Velocity vectors at sample locations generated by NSU2D for flow over NACA 23012m with 0.15" quarter round at x/c=0.10 and α=0°.